Electronic Supplementary Material (ESI) for Journal of Materials Chemistry A.


Supporting Information

# Solid oxide electrolyzer positive electrodes with novel microstructure show unprecedented stability at high current densities

*Qing Ni, Yu Li, Zongchao Zhu, Zhexiang Yu, Dong Xu, Xiaoming Hua, Yi Zhen, Lin Ge*, Lei Bi**

## Experimental details

### 1. Membrane preparation

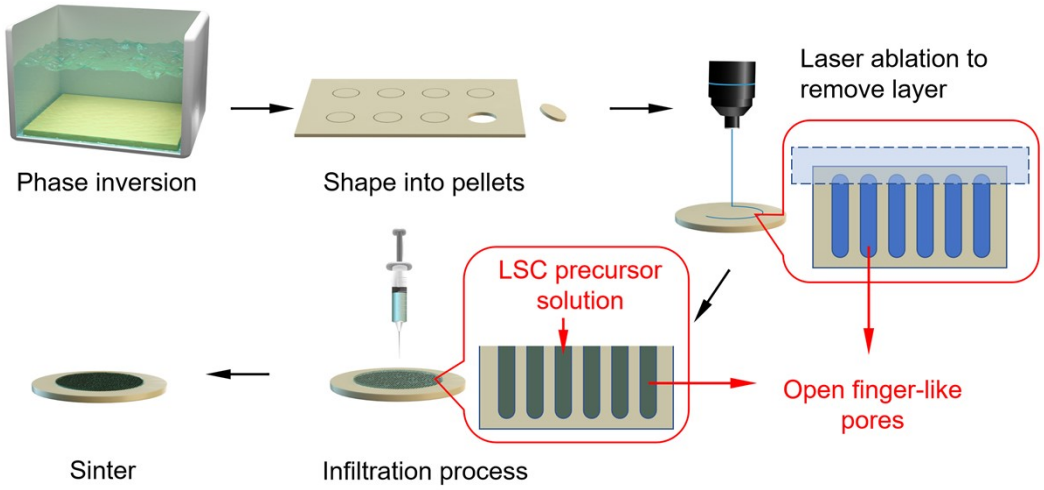


Figure S1. Preparation procedure of microchanneled YSZ substrates with LSC electrocatalyst infiltrated

### 1.1 Wettability measurement

The wettability of three different solvents on the dense YSZ substrate was studied: (1) pure water; (2) water: ethanol = 3 : 2; (3) water: n-propanol = 3 : 2. The surface tensions of the three solutions are known to be $72\times10^{-3}$, $24.5\times10^{-3}$, and $22\times10^{-3}$ N/m (at 20

°C), correspondingly. As a result, the wettabilities of the infiltration solutions to the scaffold are diverse. As shown in the Figure S2, the contact angle of the three solutions are (1) > (2) > (3). The water/ n-propanol mixture has the smallest contact angle with YSZ, exhibiting the best wettability, which means it would spread rapidly on the YSZ. Therefore, solution (3) (water: n-propanol = 3 : 2) was chosen as the mixed solvent for infiltration.

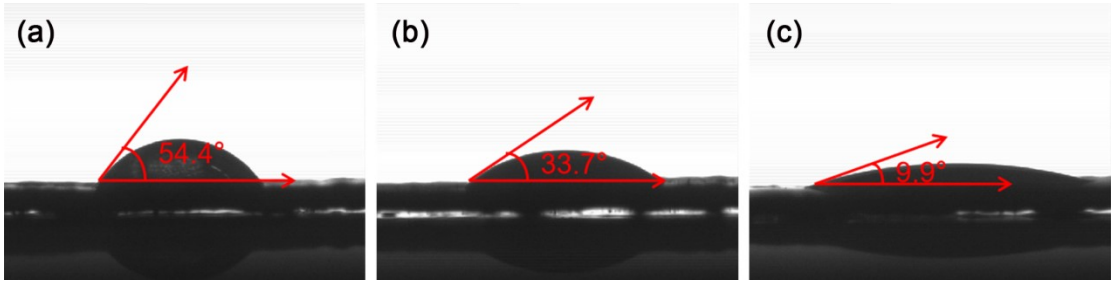


Figure S2. Wettability of three different solvents on the dense YSZ substrate: (a) pure water; (b) water: ethanol = 3 : 2; (c) water: n-propanol = 3 : 2.

**1.2 The influence of solid loadings on YSZ scaffold morphologies**

Pore growth is determined by the slurry composition, as formed through the convection of coagulant NMP and $H_2O$. The solid loading is defined as the weight ratio of YSZ to NMP+YSZ+PESf. As shown in Figure S3, YSZ scaffolds prepared with various solid loadings at a fixed PESf concentration of 10 wt% show quite different morphologies. The scaffolds obtained at solid loadings of 57 wt% and 59 wt% seem to be more efficient for gas permeation. It appears that long microchannels almost traversing the membrane are formed at a solid loading of 59 wt%, while at a solid loading of 57 wt% straight channels of tens of micrometer in diameter are gradually split into small branches from right to left. It may be related to the fact that lower solid loading leads to lower slurry viscosity, and thus more water diffusion into the skin layer along with the lowest resistance of pore growth, inducing more nuclei of polymer-poor phase as nascent pores. If the diffusion rate of water from the channels into the slurry is much slower than that of NMP into the channels, the pore channels will grow quickly. The rapidly-formed microchannel wall at the low solid loading may not be robust and could be easily collapsed during the following slow phase-inversion process. As a result,

microchannels merged into big ones with dead or enclosed microchannels possibly involved. Considering the mechanical strength as shown in Figure S4, 59 wt% is adopted as the solid loading for scaffold preparation.

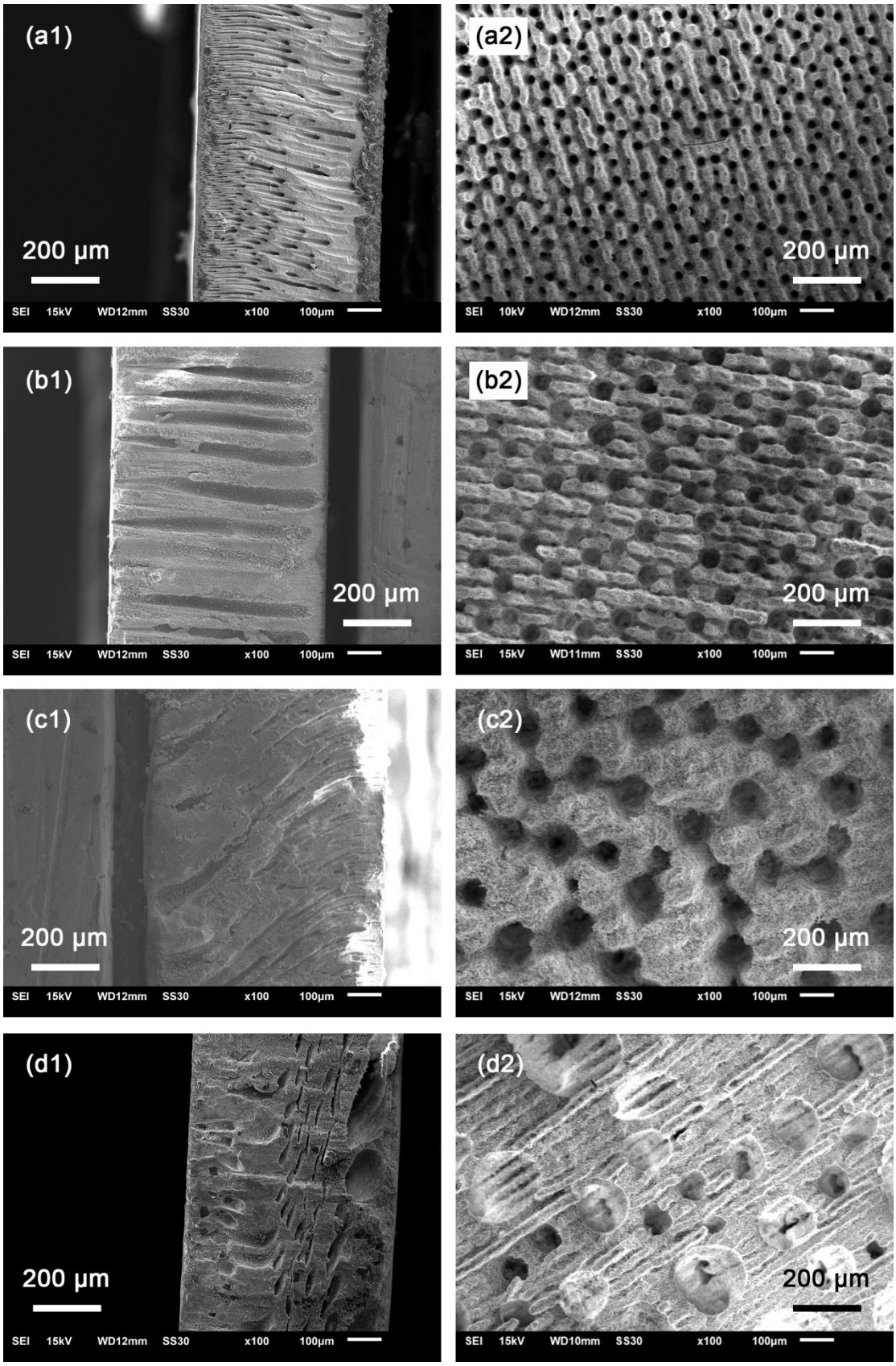


Figure S3. SEM images of cross section (a1-d1) and surface (a2-d2) of YSZ scaffolds prepared with 57% (a1 and a2), 59% (b1 and b2), 61% (c1 and c2), 63% (d1 and d2)

solid loadings

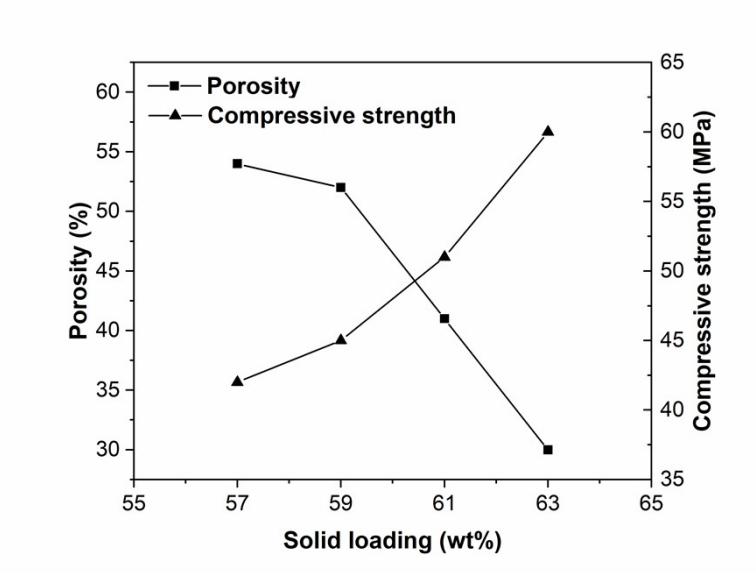


Figure S4. Porosity and compressive strength vs solid loading plots of the YSZ scaffolds

**1.3 The influence of polymer PESf concentration on YSZ scaffold morphologies**

During phase-inversion process, PESf is used as polymer to solidify the slurry. PESf concentration also influences slurry viscosity and is therefore believed to affect scaffold microstructure in a similar manner to the solid loadings. PESf concentration is defined as the weight ratio of PESf to YSZ. Figure S5 exhibits the cross sections and surfaces of membranes fabricated at various PESf concentrations. The most uniform microchannels were obtained at the PESf concentration of 10 wt%. As shown in Figure S6, it is also sufficient to meet the demands of porosity and mechanical robustness for SOECs. Therefore, the optimized PESf concentration is 10 wt%.

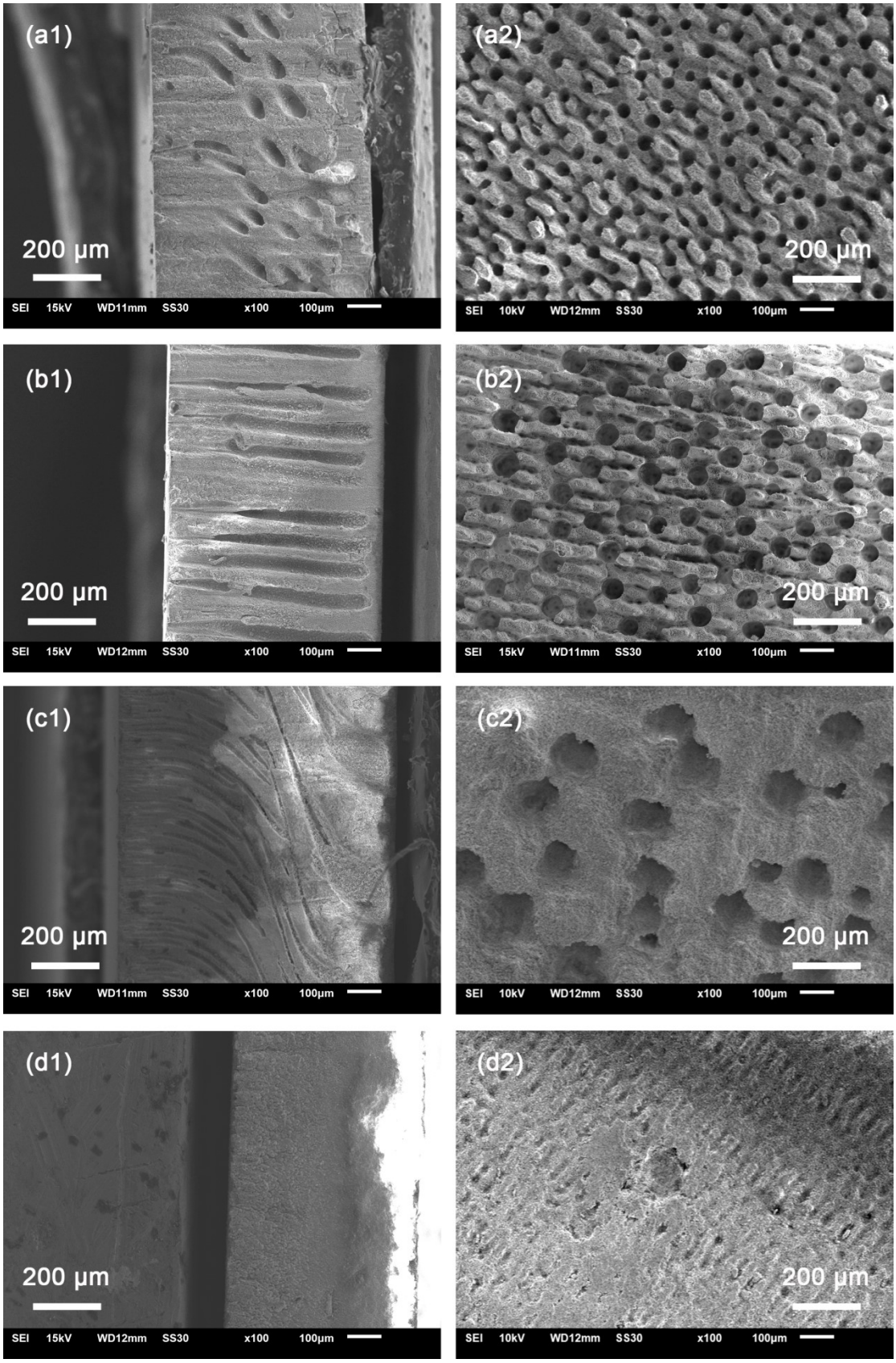


Figure S5. SEM images of cross section (a1-d1) and surface (a2-d2) of YSZ scaffolds prepared with 9% (a1 and a2), 10% (b1 and b2), 11% (c1 and c2), 12% (d1 and d2)

PESf concentrations

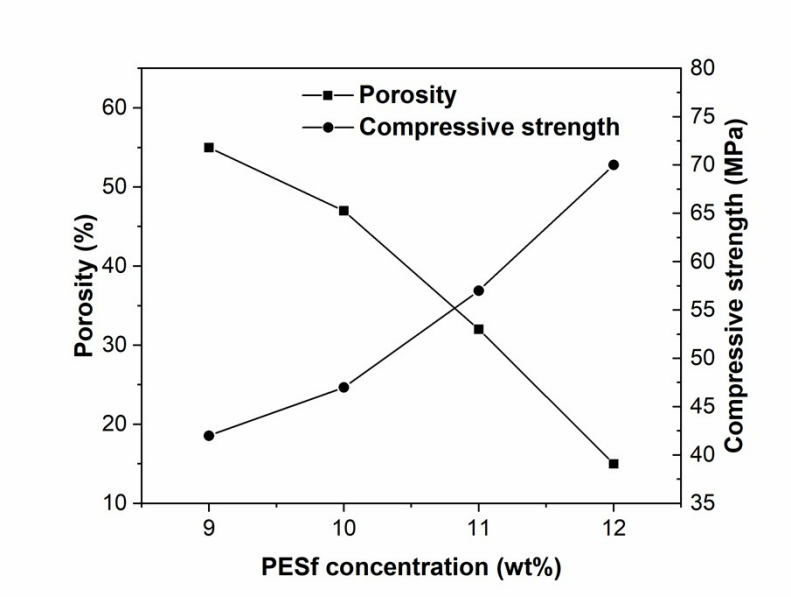


Figure S6. Porosity and compressive strength vs PESf concentration plots of the YSZ scaffolds

### 1.4 The influence of presintering temperature on YSZ scaffolds

In order to obtain robust mechanical strength and adhesion between the thin films of YSZ electrolyte and the scaffold, YSZ paste was spin-coated onto the smooth skin layer surface of the green scaffold before co-sintering. However, bending or even cracking may occur during the co-sintering process as the shrinkage of YSZ paste and green scaffold are different. Thus, the green scaffolds were presintered to adjust shrinkage. As shown in Figure S7, YSZ paste and the scaffold presintered at 1150 $^{o}$C for 2h are most compatible since they are flat without curving after co-sintered at 1400 $^{o}$C for 5h. Therefore, the presintering temperature is set as 1150 $^{o}$C.

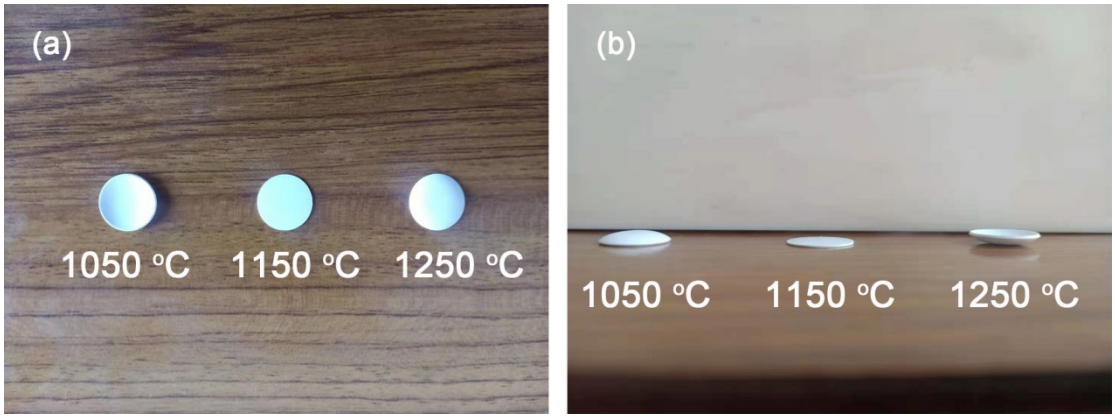

Figure S7. Digital images of YSZ scaffolds presintered at various temperatures

**1.5 The influence of polyvinyl butyral (PVB) binder on electrolyte film-forming properties**

Polyvinyl butyral (PVB) is employed as binder in YSZ electrolyte slurry. It is well known that PVB concentration has a significant effect on the viscosity of the YSZ slurry. PVB concentration is defined as the weight ratio of PVB to YSZ. As shown in Figure S8, slurry viscosity generally increases with the addition of PVB. However, both conditions, lack of or excessive PVB, would lead to flaws or cracks in electrolyte film as presented in Figure S9, which may result from isolated or accumulated YSZ particles caused by the inappropriate viscosity. Therefore, 6 wt% PVB concentration is favored in this study, where the slurry has a suitable viscosity and the formed film is smooth and even.

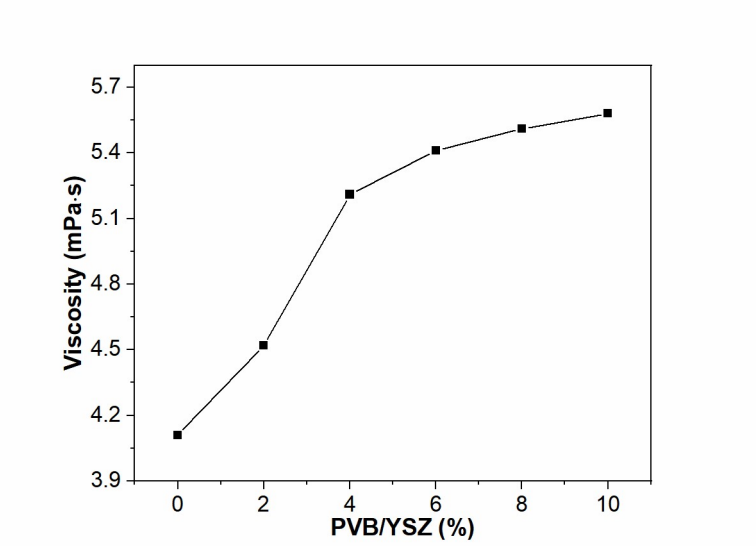


Figure S8. Plots of viscosity with different PVB concentrations

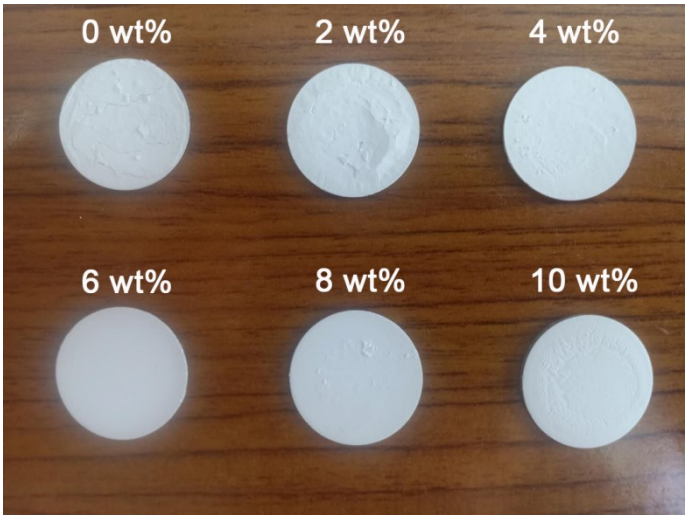


Figure S9. Digital images of electrolyte film formed with different PVB concentrations

### 1.6 The influence of electrolyte slurry solid loadings on electrolyte film-forming properties

Similar to the PVB concentration, the solid loading of electrolyte slurry also has a direct effect on electrolyte film-forming properties. The solid loading is defined as the weight ratio of YSZ to YSZ+ethanol. Figure S10 shows the slurry viscosity rises with the increment of solid loading. To investigate the effect, various solid loadings at a fixed 6 wt% PVB concentration were applied to prepare thin electrolyte membrane. It can be seen in Figure S11 that the most uniform and flat electrolyte film was formed at the solid loading of 8 wt%, which may also be attributed to the viscosity as mentioned above in section 1.5. As a result, the solid loading of electrolyte slurry is fixed at 8 wt%.

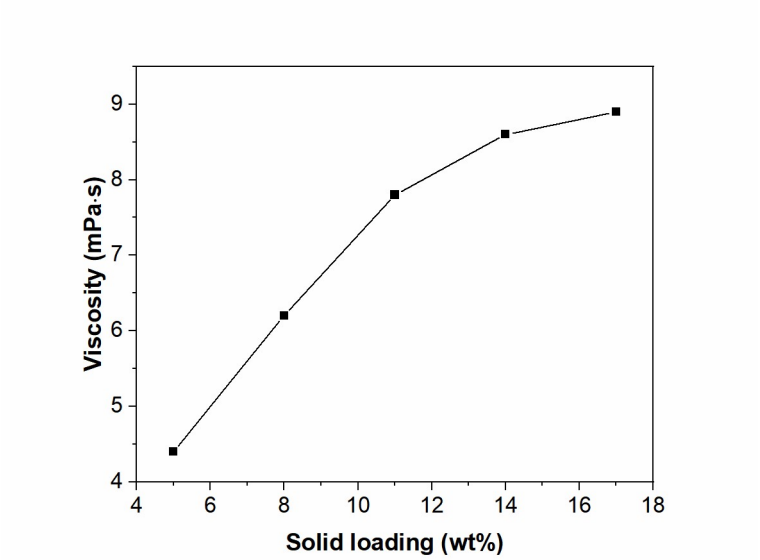


Figure S10. Plots of viscosity with electrolyte slurry of different solid loadings

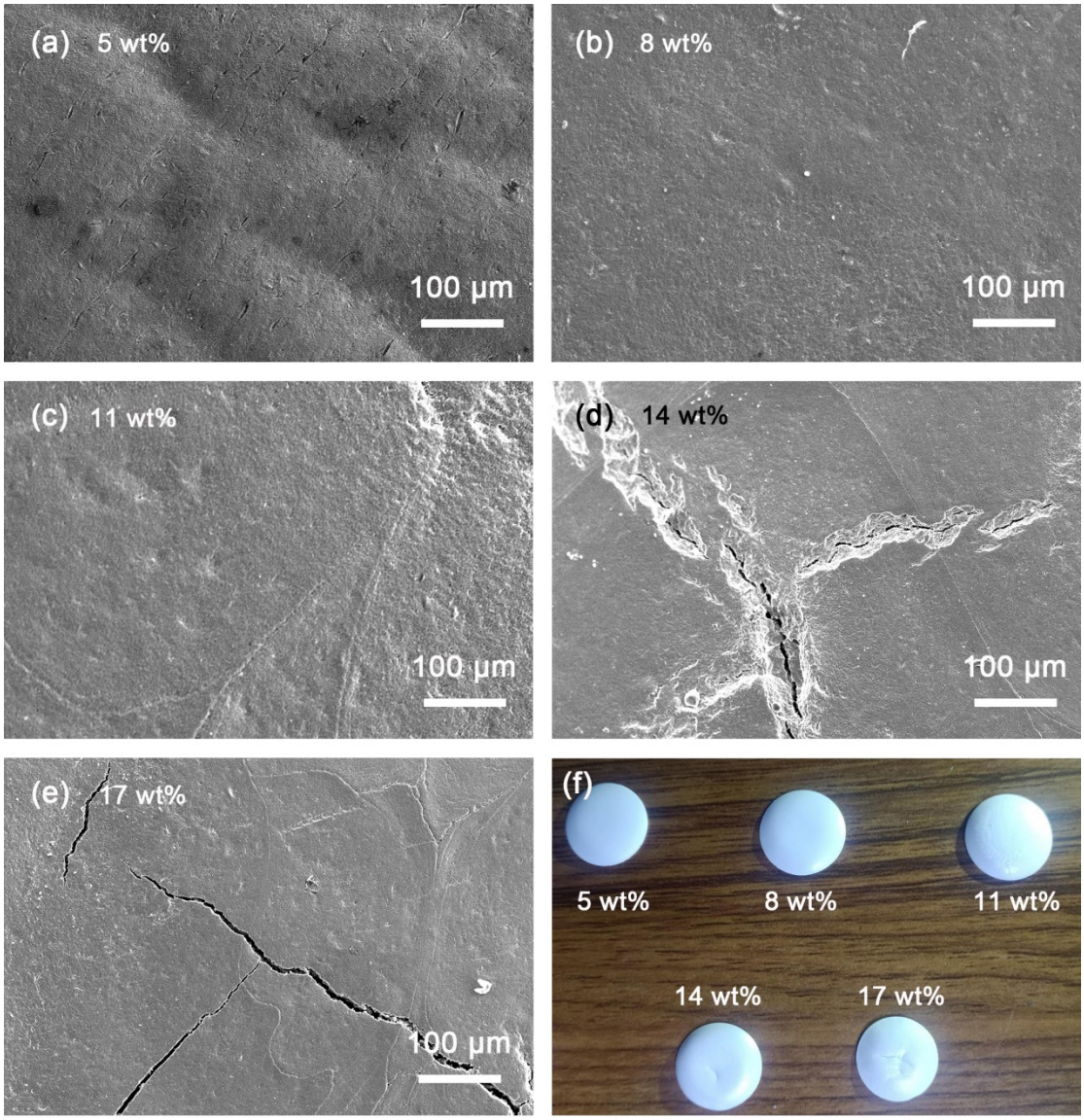


Figure S11. Images of electrolyte film formed with electrolyte slurry of different solid

loadings: (a-e) SEM images of electrolyte film surface; (f) digital image of electrolyte film

### 1.7 The influence of sintering temperature on electrolyte film

It is believed that low sintering temperature would lead to insufficient crystallinity because of limited grain growth whereas high sintering temperature would promote grain growth and thus enhance the density of the electrolyte film. Figure S12 exhibits that the YSZ electrolyte film is fully dense and well adhered to the scaffold after sintered at 1400 $^{o}$C for 5 h. Therefore the sintering temperature of electrolyte film is arranged at 1400 $^{o}$C.

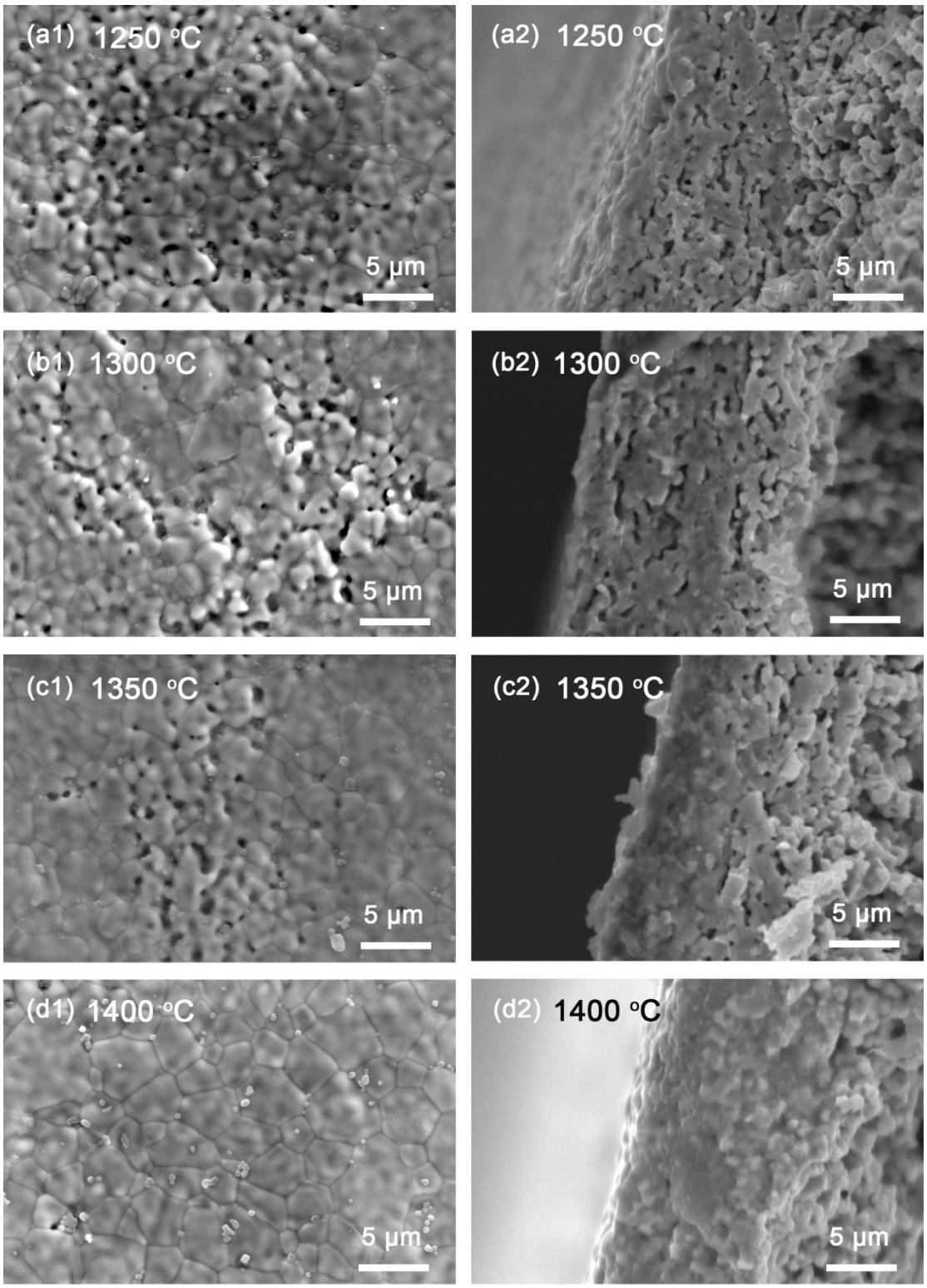


Figure S12. SEM images of surface(a1-d1) and cross-section (a2-d2) of the electrolyte film prepared at 1250 °C (a1 and a2), 1300 °C (b1 and b2), 1350 °C (c1 and c2) and 1400 °C (d1 and d2) co-sintering temperatures

### 1.8 Effects of coating methods on electrolyte film

Drop coating and spin coating are simple and efficient methods of preparing thin electrolyte film on smooth surface of scaffold. As shown in Figure S13, there is an apparent dividing line between the electrolyte and the YSZ scaffold after drop coating and drying process while a good adhesion is obtained via spin coating method. Furthermore, some isolated pores are formed in the electrolyte film fabricated by drop coating whereas the spin-coating electrolyte film is relative dense. It is well know that pores in electrolyte may have an adverse impact on ionic conductivity. These may be attributed to vacuum pressure assistance in spin coating process, which provides an external driving force for particle sedimentation and effectively remove the bubbles across the coating. In addition, the thickness of both the green and sintered electrolyte film via spin coating is much smaller than that by means of drop coating, while the shrinkage of the electrolyte film through spin coating is almost twice as much as that by means of drop coating. All the mentioned above indicate that electrolyte film prepared by spin coating tends to be thinner and denser.

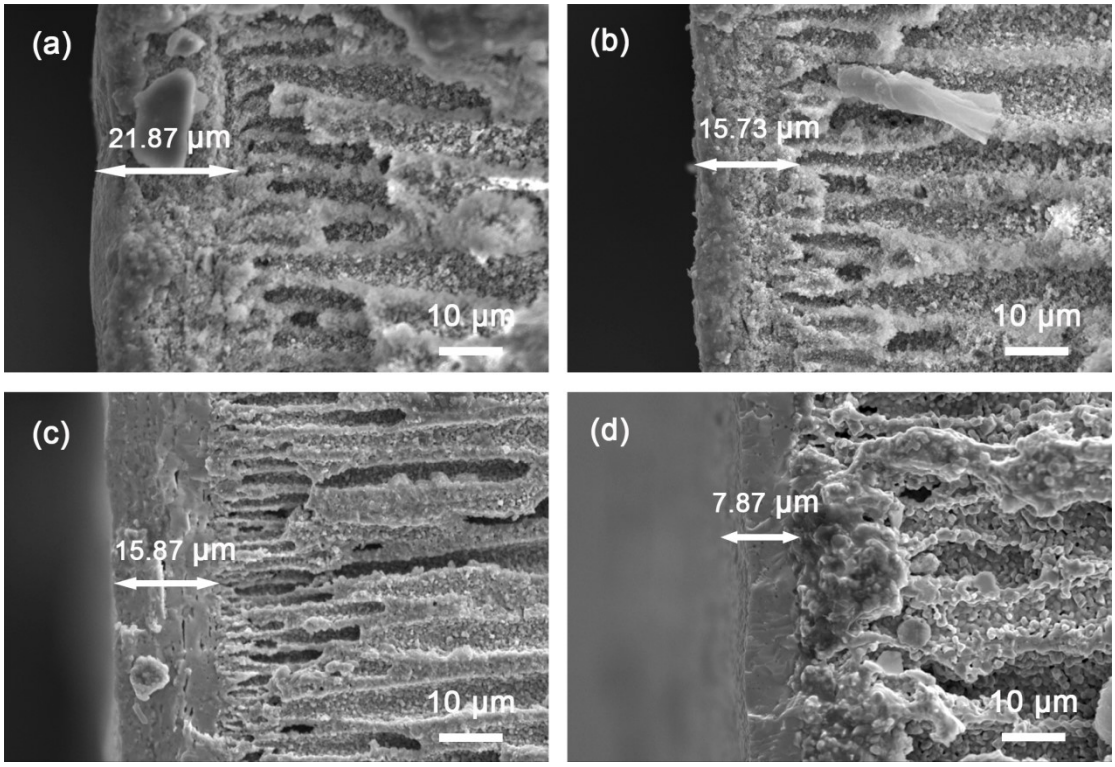


Figure S13. SEM images of cross-section of electrolyte film prepared by: (a)drop coating before sintering; (b) spin coating before sintering; (c) drop coating after

sintering; (d) spin coating after sintering

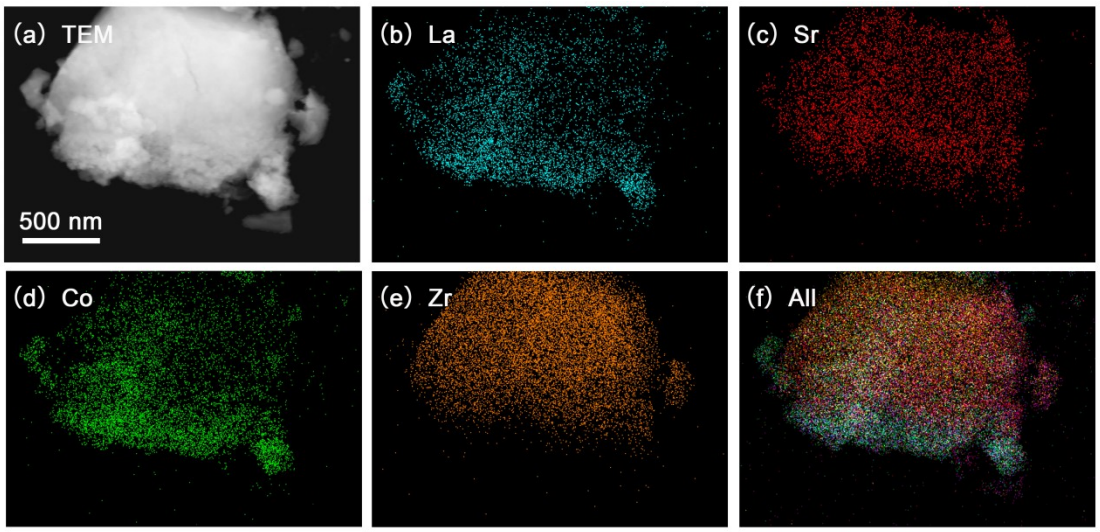


Figure S14. TEM image of LSC nanoparticles on the internal channel surface of the YSZ scaffold and the elements distributions. (a) TEM image of LSC nanoparticles. (b), (c), (d) and (e) EDS mapping images of the distribution of La, Sr, Co Zr and all elements investigated by TEM, respectively. (f) Mapping images of the all elements distribution; the blue, red, green, orange and pink zone represent the distribution of La, Sr, Co, Zr and O, respectively.

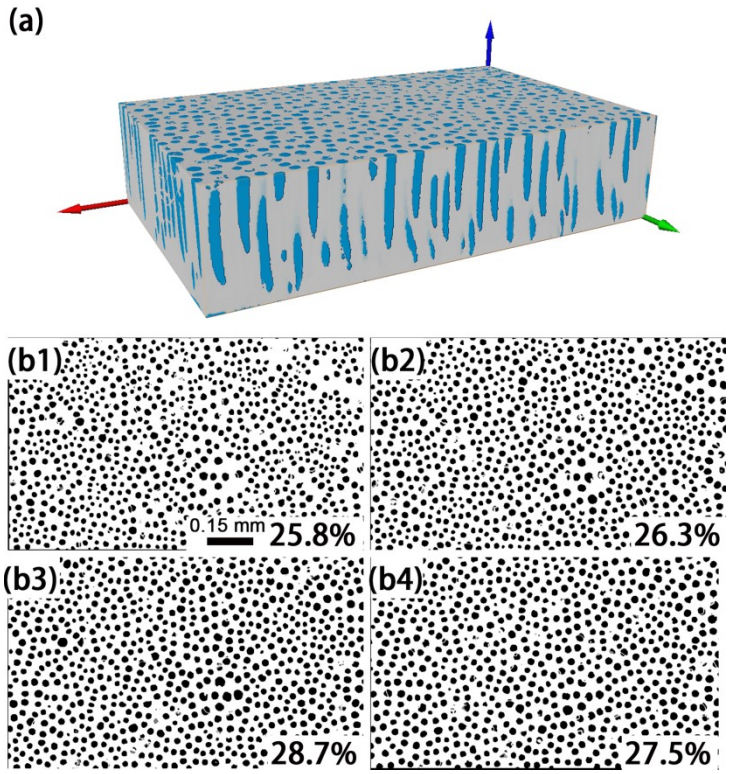


Figure S15. (a) CT-reconstructed 3D image of the microchanneled scaffold of the tested Cell #4 sample. (b) Representative slices with void area (black) percentages at different positions in Z direction: (b1-b4) z=0.05, 0.10, 0.15 and 0.20 mm of the channeled anode.

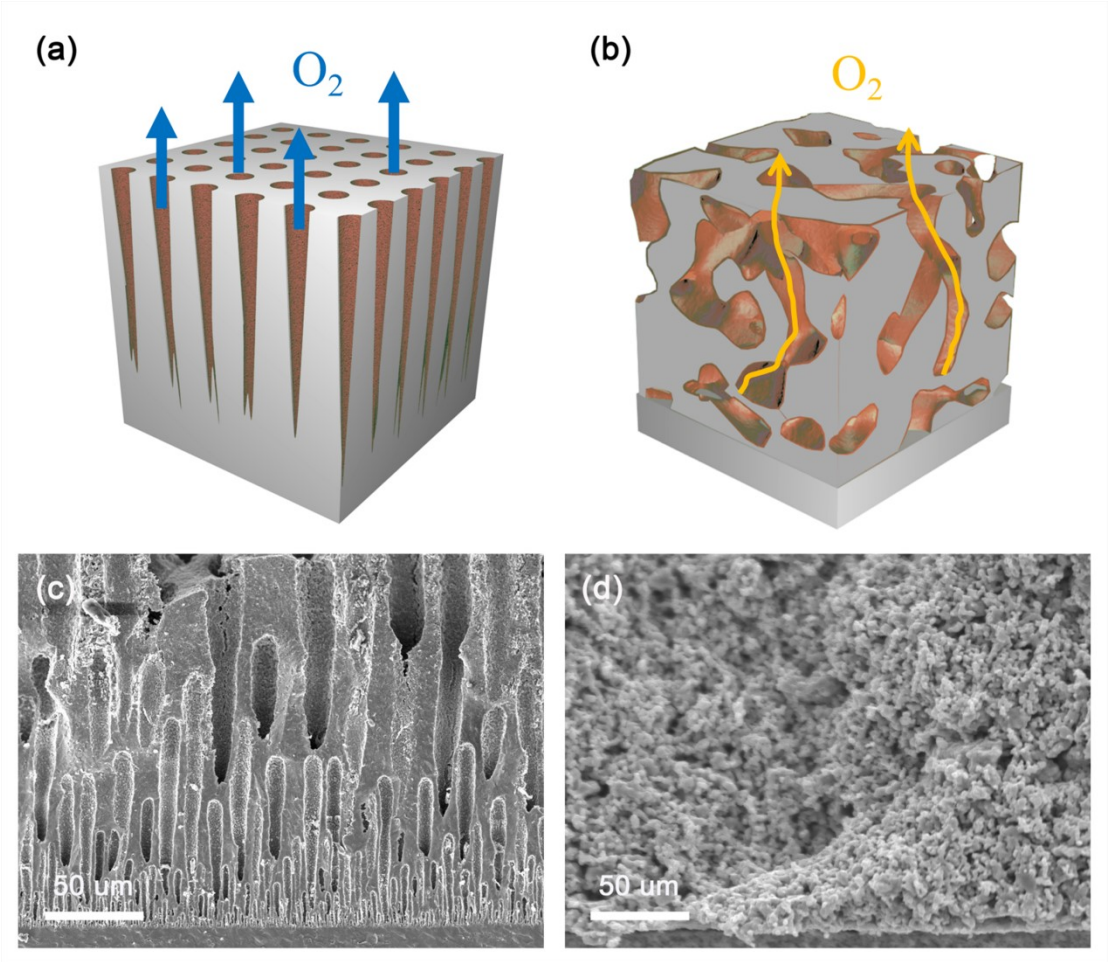


Figure S16. Comparison of (a, c) microchanneled anode and (b, d) traditional porous anode for SOECs. (a, b) Schematic representation of oxygen release pathway within anode supports. (c, d) SEM images of anodes.